Eastward Shift of Interannual Climate Variability in the South Indian Ocean since 1950

Lei Zhang[1], Weiqing Han[1], Kristopher B. Karnauskas[1,2], Yuanlong Li[1,3], Tomoki Tozuka[4]

1 Department of Atmospheric and Oceanic Sciences, University of Colorado, Boulder, Colorado, USA

2 Cooperative Institute for Research in Environmental Sciences, University of Colorado Boulder, USA

3 CAS Key Laboratory of Ocean Circulation and Waves, Institute of Oceanology and Center for Ocean Mega-Science, Chinese Academy of Sciences, Qingdao, China

4 Department of Earth and Planetary Science, Graduate School of Science, University of Tokyo, Tokyo, Japan

Revised manuscript submitted to *Journal of Climate*

***Corresponding author:**

Lei Zhang

Department of Atmospheric and Oceanic Sciences,

University of Colorado, Boulder, CO 80302, USA

Email: lezh8230@colorado.edu

Abstract

The subtropical Indian Ocean Dipole (SIOD) and Ningaloo Niño are the two dominant modes of interannual climate variability in the subtropical South Indian Ocean. Observations show that the SIOD has been weakening in the recent decades, while Ningaloo Niño has been strengthening. In this study, we investigate the causes for such changes by analyzing climate model experiments using the NCAR Community Earth System Model version 1 (CESM1). Ensemble-mean results from CESM1 large-ensemble (CESM1-LE) suggest that the external forcing causes negligible changes in the amplitudes of the SIOD and Ningaloo Niño, suggesting a dominant role of internal climate variability. Meanwhile, results from CESM1 pacemaker experiments reveal that the observed changes in the two climate modes cannot be attributed to the effect of sea surface temperature anomalies (SSTA) in either the tropical Pacific or tropical Indian Oceans. By further comparing different ensemble members from the CESM1-LE, we find that a Warm Pool Dipole mode of decadal variability, with opposite SSTA in the southeast Indian Ocean and the western-central tropical Pacific Ocean plays an important role in driving the observed changes in the SIOD and Ningaloo Niño. These changes in the two climate modes have considerable impacts on precipitation and sea level variabilities in the South Indian Ocean region.

Key words: Indian Ocean; Subtropical Indian Ocean Dipole; Ningaloo Niño; Warm Pool Dipole;

1. Introduction

Modes of coupled climate variability are defined by recurring patterns of variations in large-scale atmospheric and oceanic conditions, including winds, precipitation, sea level, and sea surface temperature (SST) (McPhaden et al. 2006; Saji et al. 1999; Webster et al. 1999). Through modulating regional environmental conditions both locally and remotely, climate modes are known to modulate extreme weather events, such as extreme precipitation (Higgins et al. 2011; Denniston et al. 2015), cold air outbreaks and heat waves (e.g., Ratnam et al. 2016; Lin et al. 2018), and tropical cyclone activity (e.g., Wang and Chan 2002; Jin et al. 2014). Hence, modes of interannual climate variability are the major source of predictability for seasonal climate forecasts. Understanding their low-frequency changes may help improve climate prediction and thus has large societal benefits.

Nations surrounding the Indian Ocean are home to one third of the global human population, and most of them are developing countries that are especially vulnerable to changes in regional environmental conditions (Han et al. 2014b, 2019). In addition, Indian Ocean climate variability and change have remote climatic impacts on regions around the globe through atmospheric teleconnections and inter-basin interactions (Hoerling and Kumar 2002; Saji and Yamagata 2003; Yang et al. 2007; Xie et al. 2009; Luo et al. 2012; Han et al. 2014a; Zhang and Han 2018; Zhang et al. 2019a; Cai et al. 2019; Hu and Fedorov 2019; Zhang et al. 2021). Therefore, it is important to better understand the linkages between modes of climate variability in the Indian Ocean and their decadal evolutions.

In the subtropical South Indian Ocean, the dominant interannual climate mode is the subtropical Indian Ocean Dipole (SIOD) (Behera and Yamagata 2001), manifest as a dipole-like SST anomaly (SSTA) pattern between the regions to the southeast of Madagascar islands and west of Australia. The negative phase of the SIOD is associated with cold SSTA in the western and warm SSTA in the eastern South Indian Ocean, together with large-scale cyclonic wind anomalies over the subtropical basin suggesting weakened Mascarene High (Figs. 1b and 1c). The SIOD can also induce prominent regional sea level variations in the South Indian Ocean (Zhang et al. 2019b) and significantly affect southern African rainfall (Behera and Yamagata 2001; Reason 2001; Zhang et al. 2019b).

The other major climate mode in the South Indian Ocean is Ningaloo Niño (Feng et al. 2013), which is a long-lasting marine heatwave (Pearce and Feng 2013; Caputi et al. 2014; Holbrook et al. 2020) characterized by warm SSTA extending from the west coast of Australia into the central tropical Indian Ocean (Fig. 1a). Ningaloo Niño is associated with a prominent coastal sea level increase and significant rainfall changes over Australia (Feng et al. 2013; Tozuka et al. 2014; Zhang et al. 2018a). The warm SSTA associated with Ningaloo Niño is primarily caused by the coastal northerly wind anomalies that weaken the mean state southerly winds (Kataoka et al. 2014); in turn, the warm SSTA may enhance the anomalous northerlies through causing cyclonic wind anomalies to the west as an atmospheric Rossby wave (Tozuka et al. 2014, 2021). Hence, local large-scale air-sea interaction plays a crucial role in the formation of Ningaloo Niño (Zhang et al. 2018a; Tozuka and Oettli 2018; Guo et al. 2020).

Development of Ningaloo Niño is sometimes associated with the tropical Pacific forcing, with cold SSTA in the western tropical Pacific playing a more important role compared to the eastern tropical Pacific (Marshall et al. 2015; Feng et al. 2021). Indeed, warm SSTA in the southeast Indian Ocean associated with Ningaloo Niño tend to co-occur with cold SSTA in the central-western tropical Pacific (Fig. 1a). Recently, it has been found that the SSTA in these two regions can amplify each other through inter-basin interactions via both atmospheric and oceanic connections (Zhang and Han 2018): The southeast Indian Ocean warming can strengthen the central-western tropical Pacific easterly trade winds which subsequently induce cooling anomalies through enhancing surface evaporation, oceanic upwelling and anomalous cold advection; in turn, the cold SSTA may amplify the southeast Indian

Ocean warming through strengthening the surface cyclonic winds (weakening the coastal southerly winds) and the Indonesian-throughflow (ITF) (Clarke and Liu 1994; Meyers 1996; Feng et al. 2013; Kataoka et al. 2014; Li et al. 2017; Zhang et al. 2018a; Tozuka et al. 2014). This mode of interbasin coupling has been referred to as the Warm Pool Dipole (WPD) because of its proximity to the Indo-Pacific Warm Pool region (Zhang and Han 2020).

The SIOD and Ningaloo Niño exhibit some similarities in terms of their spatial patterns of SST and surface wind anomalies (Fig. 1). For instance, Ningaloo Niño is associated with weak cold SSTA to the west of the warm SSTA, resembling the SIOD but with the overall pattern shifted to the eastern basin for Ningaloo Niño. Similarly, both climate modes are associated with cyclonic wind anomalies over the subtropical South Indian Ocean to the west of their warm poles, except that they are centered at different longitudes. Additionally, they both peak during austral summer. These results indicate that the SIOD and Ningaloo Niño may either be intrinsically linked, or simply project onto one another in a confounding fashion. In addition, observations show that the SIOD has weakened since 1950 (Yan et al. 2013; Zhang et al. 2019b), while Ningaloo Niño has strengthened (Fig. 2a, d, g) (Zinke et al. 2014; Feng et al. 2015a). Indeed, the overall SSTA standard deviation (SD) has been decreasing in the subtropical South Indian Ocean, while increasing along the west Australian coast (Fig. 2c, f, i), implying an overall eastward shift of the action centers for interannual climate variability in the South Indian Ocean. Here the action center refers to the region where the SSTA SD is large during certain periods (e.g., “X”s marked in Fig. 3), representing the region where prominent interannual climate anomalies associated with these modes preferentially occur. Given the prominent climatic and ecological impacts of both climate modes (Byrne 2011; Depczynski et al. 2013), it is important to explore the causes for their changes in recent decades. While the strengthening of Ningaloo Niño has been attributed to the effects of anthropogenic global warming and the phase shift of the Inter-decadal Pacific Oscillation (IPO) (Feng et al. 2015b), their relative roles have not been quantified. Causes for the weakening of the SIOD have not been explored either. In this study, we investigate the physical mechanisms for the observed changes in amplitudes of the SIOD and Ningaloo Niño since the 1950s, and examine effects of these changes on climate conditions over the South Indian Ocean and surrounding regions.

The rest of this paper is organized as follows. Section 2 describes the observational data sets and model experiments analyzed in this study, section 3 explores the causes for the changes in the SIOD and Ningaloo Niño, section 4 investigates the associated impacts on precipitation and sea level, and section 5 summarizes the major findings of this study.

2. Methods and data

To examine the changes of the SIOD and Ningaloo Nino, we analyze multiple observational SST data sets including the Hadley Centre Sea Ice and SST data set version 1.1 (HadISST, 1˚x1˚, Rayner et al. 2003), Centennial in situ Observation-Based Estimates (COBE1) SST data (1˚x1˚, Ishii et al. 2005), and National Oceanic and Atmospheric Administration (NOAA) Extended Reconstructed SST version 5 (ERSSTv5, 2˚x2˚, Huang et al. 2017). The analysis period is 1950-2018. To analyze large-scale wind, precipitation and sea level anomalies associated with the two climate modes, we use the European Centre for Medium-Range Weather Forecasts (ECMWF) Twentieth Century Reanalysis (ERA-20C, Poli et al. 2016) for 1950-2010 and ECMWF Ocean Reanalysis System 4 (ORAS4, Balmaseda et al. 2013) for 1958-2017. For comparison, atmospheric data from National Centers for Environmental Prediction Reanalysis 1 (NCEP1; Kalnay et al. 1996) for 1950-2018 and satellite-derived daily sea level product during 1993-2018 obtained from Copernicus Marine Environment Monitoring Service (CMEMS) are also analyzed. Since we find that results from the two reanalysis data sets are quite similar (e.g., Figs. 1 and S1), we primarily show the ERA-20C results in this study. To remove the anthropogenic global warming effect, regression on the global mean SSTA has been removed from all anomaly fields (Zhang et al. 2021).

To document the time evolution and analyze large-scale climate anomalies associated with the SIOD, we define the subtropical dipole mode index (SDMI) as domain-averaged SSTA differences between 55˚–65˚E, 37˚–27˚S and 90˚–100˚E, 28˚–18˚S (Fig. 1b) (Behera and Yamagata 2001). Similarly, we define the Ningaloo Niño index (NNI) as the SSTA averaged over (22˚–16˚S,102˚–108˚E and 32˚–16˚S, 108˚–115˚E) (Fig. 1a) (Zhang et al. 2018a).

To explore the relative roles of external radiative forcing (both natural and anthropogenic) and internal climate variability in causing the changes in the South Indian Ocean interannual climate variability, we analyze the National Center for Atmospheric Research (NCAR) Community Earth System Model version 1 (CESM1; Hurrell et al. 2013) large-ensemble (CESM1-LE) (Kay et al. 2015) that has 40 members. In addition, we also analyze two sets of pacemaker experiments using the same configurations as the CESM1-LE, but with the SSTA in the central-eastern tropical Pacific and tropical Indian Ocean restored to observed values respectively (Fig. S2). Both pacemaker experiments have 10 ensemble members that are initialized with slightly perturbed initial conditions. Hereafter, the Pacific pacemaker experiment is referred to as Pacific Ocean-Global Atmosphere (POGA) experiment, and Indian Ocean-Global Atmosphere (IOGA) for the Indian Ocean pacemaker experiment. More details about the two pacemaker experiments can be found in Schneider and Deser (2018) and Zhang et al. (2019a).

All three sets of CESM1 experiments are for the period 1950-2018, during which time the Coupled Model Intercomparison Project Phase 5 (CMIP5) historical forcing is applied for 1920-2005, and Representative Concentration Pathway 8.5 (RCP8.5) forcing scenario is used for 2006-2018. The only difference of the external forcing between the CESM1-LE and the two pacemaker experiments is the ozone: Ozone forcing from Whole Atmosphere Community Climate Model (Marsh et al. 2013) is used in CESM1-LE, while POGA and IOGA are forced by Stratosphere-Troposphere Processes and Their Role in Climate (Eyring et al. 2013) ozone data. The different ozone forcing does not cause significant differences in the region analyzed in this study (e.g., Schneider et al. 2015). Since the internal climate variability (outside the nudging region in the pacemaker experiments) is not synchronous across different ensemble members in the CESM1 experiments due to different initial conditions, the CESM1 ensemble mean results may filter out its effect. As a result, the CESM1-LE ensemble average isolates the effect of external forcing, while the ensemble-mean results from POGA and IOGA are due to the combined effects of both external forcing and the SSTA forcing in the tropical Pacific and Indian Ocean respectively.

3. Changes in the South Indian Ocean interannual climate variability

3.1 Weakened SIOD and strengthened Ningaloo Niño

The 11-year running variance of the December-February (DJF) mean SDMI exhibits an overall decreasing trend (–0.01 yr^{-1}) in all three observational SST data sets, while the DJF NNI variance has been persistently increasing especially since 2000 (0.024 yr^{-1}) (Fig. 2b, e, h). The trends of the running variance of both indices are statistically significant at the 99% confidence level, except for the trend of the SDMI variance in COBE1, which is only significant at the 80% confidence level. Given that the SIOD is the dominant mode in the central subtropical basin and Ningaloo Niño, the southeast Indian Ocean, it is also clear that the SSTA SD has decreased in the SIOD poles and increased in the Ningaloo Niño region (Fig. 2c, f, i). In fact, due to the contrasting changes in the amplitudes of the SIOD and Ningaloo Niño, the empirical orthogonal function (EOF) analysis of the South Indian Ocean SSTA shows that the SIOD is the first dominant EOF (EOF1) mode prior to 1985, whereas Ningaloo Niño becomes the EOF1 mode since then (Fig. S3). We also notice that there are EOF modes that are associated with neither the SIOD nor the Ningaloo Niño, with large EOF loadings in the subtropical (20˚S-40˚S) or mid-latitude South Indian Ocean (30˚S-50˚S). It is interesting to investigate in detail the causes for these EOF modes, but since we mainly focus on SIOD and Ningaloo Niño in this study, the leading EOF mode for the two periods respectively, other EOF modes will not be discussed any further.

We also note that the correlations between the SIOD and Ningaloo Niño are low during the 1950s-1970s and since 1990, but high for 1980-1990 peaking in the early 1980s (Fig. 2b, e, h). As mentioned above, the spatial patterns of SSTA associated with the SIOD and Ningaloo Niño project onto each other, albeit with a subtle zonal shift (Fig. 1), suggesting a potential intrinsic linkage between the two. For instance, when the SIOD pattern is shifted/extended eastward, it may be associated with warm SSTA in the western Australian coasts, leading to a positive NNI (Figs. 1a and 1b). Hence, as the action center for the interannual climate variability (represented by the large SSTA SD center) shifts eastward in the South Indian Ocean (Fig. 3), the associated large-scale climate anomalies (e.g., cyclonic wind anomalies and the SSTA dipole) preferably occur in the region between the typical SIOD and Ningaloo Niño regions during the 1970s and 1980s. As a result, the two modes are entangled together, leading to a temporary high correlation between them.

Interestingly, the eastward shift of the action center exhibits stepwise changes, with the maximum center located at the western basin during the 1950s and 1960s, the central basin during the 1970s and early-1980s, and the eastern basin coastal region since 1990 (Fig. 3). Such stepwise changes are because SIOD and Ningaloo Niño tend to only occur in certain regions, as revealed by the EOF results showing that the two modes remain located in the same regions during different periods, despite significant changes in their relative strength (Fig. S3). Also note that although location of the SIOD has not changed, SSTA at its western pole has been weakening while its eastern pole has been strengthening based on the EOF results for different time periods (Figs. S3 and S4). Consequently, the action center has moved from the western pole to the eastern pole of the SIOD, and then to the coastal Ningaloo Niño region, manifest as a stepwise shift in the large SSTA SD center associated with changes in the two modes. Since the SSTA SD (Fig. 3) as well as the SDMI and NNI (Fig. 2) exhibit more significant changes near 1985 compared to that near 1970 (Fig. 2), hereafter we use the year 1985 as the dividing line to define two periods for our analysis. The trend pattern of the 11-year running SSTA SD (Fig. S5) is indeed similar to the differences in the SSTA SD between pre-1985 and post-1985 periods (Fig. 2), suggesting that it is appropriate to use the two time periods to investigate changes in the South Indian Ocean climate variability.

Since the remote Pacific influences may strongly affect Indian Ocean climate conditions, we then examine changes in both SSTA and its SD in the entire tropical Indo-Pacific region between pre-1985 and post-1985 periods (Fig. 4). Compared to earlier periods, all three observational SST data sets show prominent low-frequency dipole-like SSTA between the southeast Indian Ocean and the central-western tropical Pacific Ocean (Fig. 4, right column). Hence, similar to the interannual WPD, this is also a dipole-like SSTA pattern in the Indo-Pacific warm pool region but on decadal to multi-decadal timescales, which is therefore referred to as *decadal* WPD hereafter. In addition, observations also show enhanced ENSO variability, particularly at the central equatorial Pacific Ocean (Fig. 4, left column), which is consistent with the recent strengthening of the central-Pacific El Niño (Lee and McPhaden 2010). To explore the processes that cause the contrasting changes in the SIOD and Ningaloo Niño, and investigate whether and how the tropical Pacific remote forcing may have contributed, next we analyze the different CESM1 experiments.

3.2 Causes for recent changes in the two climate modes

Changes in the SIOD and Ningaloo Niño in recent decades could be due to the effects of external forcing (both natural and anthropogenic) and/or internal climate variability. To examine the relative roles of different mechanisms in contributing to the observed changes in the two climate modes, we analyze climate model simulations using CESM1 that separate possible mechanisms. We first compare the anomaly patterns associated with the SIOD and Ningaloo Niño in observations and CESM1-LE to evaluate the model performance in simulating them (Figs. 5 and S6). Results show that the CESM1 can sufficiently reproduce the SST, sea level, and wind anomalies in the South Indian Ocean associated with the two modes, as well as their connections with Pacific SSTA. For instance, the La Niña-like SSTA pattern with negative sea level anomalies in the central-eastern tropical Pacific during Ningaloo Niño is well captured by the model; both the SIOD SSTA dipole and the associated north-south dipole-like sea level anomalies in the western South Indian Ocean (Zhang et al. 2019c) are reproduced by the model as well. However, there are some noticeable model biases, especially in the tropical Indian Ocean. While the observed SIOD and Ningaloo Niño are not associated with significant anomalies in the tropical Indian Ocean, CESM1 simulates prominent cold SSTA and negative sea level anomalies in the western tropical Indian Ocean associated with Ningaloo Niño. Additionally, observations show prominent warm SSTA and higher sea level in the central tropical Pacific during the negative SIOD, while the model underestimates such signals. Despite these model biases, we suggest that CESM1 overall renders a sufficient simulation of the relevant variability.

We use various CESM1 experiments to isolate the roles of external forcing and internal climate variability. We first analyze ensemble members from the CESM1-LE, the ensemble mean signals of which are solely due to the common external forcing and have been removed prior to calculating the SSTA SD since we focus on changes in the internal climate variability. The averaged CESM1-LE results simulate minimal changes in the amplitudes of the SIOD and Ningaloo Niño in recent decades (Fig. 6a), with changes in the SD of Ningaloo Niño and the SIOD only differing by 0.01 ˚C on average, which is much smaller than the observed values that range from 0.08 (COBE, circle in Fig. 6) to 0.19 ˚C

(ERSSTv5, square). Note that to better represent changes in the action center, here we use the area averaged SSTA SD to represent the SIOD strength, rather than using the SDMI itself. Hence, external radiative forcing does not seem to play a major role in causing the observed contrasting changes in the two climate modes. On the other hand, the spread across different ensemble members due to the influences of internal climate variability is quite large (Fig. 6a, right panel). We further analyzed simulations from 29 climate models that participate the Coupled Model Intercomparison Project Phase 5 (CMIP5), and found that they tend to simulate strengthened SSTA SD in both the Ningaloo Niño and the SIOD regions (Fig. S7) and therefore cannot capture the contrasting changes in the two modes either. Note that the spread across CMIP5 models is due to influences of both internal climate variability and cross-model differences. These results suggest that the recent changes of the South Indian Ocean interannual climate variability are likely dominated by the effect of internal climate variability.

Next, we analyze the two sets of the CESM1 pacemaker experiments to examine the effects of internal climate variability in the tropical Indian and Pacific Oceans, since both of them have been suggested to prominently affect the South Indian Ocean climate (e.g., Feng et al. 2013; Zhang et al. 2018). Ensemble mean signals from the CESM1-LE have been removed from the pacemaker experiments to exclude influences of the external forcing. Ensemble mean results of the POGA experiments, which isolate the effect of the tropical central-eastern Pacific (east of the dateline) SSTA (Fig. S2), indeed show strengthening of Ningaloo Niño (Fig. 6b), but the amplitude of such change is at the low end of the observed values, and it fails to capture the weakening of the SIOD. Differences between POGA ensemble mean changes in the SD of the two climate modes is only 0.001˚C, suggesting that the tropical Pacific remote forcing may contribute to but cannot fully explain the recent contrasting changes of the two South Indian Ocean climate modes. The ensemble mean of the IOGA experiments, which isolates the effect of the tropical Indian Ocean SSTA, similarly misses the observed weakening of the SIOD. These results show that internal climate variability within the tropical Indian Ocean and the central-eastern tropical Pacific alone cannot fully explain the observed changes of the SIOD and Ningaloo Niño.

What internal climate variability may lead to the recent eastward shift of the action center for the South Indian Ocean interannual climate variability? To answer this question, we compared the differences between the ensemble members from the CESM1-LE that do and do not simulate both the weakening of the SIOD and the strengthening of Ningaloo Niño (Fig. 7a). Note that unlike the small changes in the SSTA SD in the ensemble mean results from the CESM1-LE, changes of the SSTA SD in the composites of the selected ensemble members are comparable to observations (Figs. 4, 6 and 7). In addition, the large SSTA SD center also exhibits eastward shift during the analysis period in these ensemble members (Fig. 8), bearing some resemblance to observational results. On the other hand, the CESM1-LE composite shows significantly enhanced SSTA SD in the tropical Indian Ocean, which is absent in the observational results. This is likely due to the model bias in simulating too strong tropical Indian Ocean SSTA associated with Ningaloo Niño (Figs. 1a and 5a).

Corresponding to the changes in the South Indian Ocean internal climate variability, model results show a decadal WPD pattern with opposite SSTA between the southeast Indian Ocean and the western tropical Pacific Ocean, which is similar to the observations but with the overall pattern shifted westward (Figs. 4 and 7). For instance, the Pacific cold SSTA are mainly found at the central tropical Pacific Ocean in observations, while the model shows largest cooling to the west of the date line. The southeast Indian Ocean warming center in the model is also located to the west of the typical Ningaloo Niño region. Similarly, the interannual WPD pattern also extends further to the west in the CESM1-LE compared to the observations (Figs. 1a and 5a). Hence, these model-data discrepancies could be due to model biases in simulating the interbasin coupled pattern associated with the WPD. In addition, interferences from the IPO, the phase of which is not synchronous in the various ensemble members of the CESM1-LE and is thus filtered out in the ensemble mean model results but exists in observations, may also contribute to the model-data difference in the SSTA pattern. Meanwhile, SST has been cooling (warming) in the western (eastern) tropical Indian Ocean in observations (Fig. 4), which is opposite to those in the selected CESM1-LE members (Fig. 7b). However, since the IOGA experiments that isolate the impact of the observed tropical Indian Ocean SSTA cannot reproduce the observed contrasting changes of the SIOD and Ningaloo Niño, this model-data difference does not seem to play a major role.

The effect of the decadal WPD SSTA on the South Indian Ocean is likely initiated by the positive SSTA in the southeast Indian Ocean. As mentioned above, both SIOD and Ningaloo Niño are associated with large-scale local atmosphere-ocean interactions, which are promoted by the higher background SST that makes it easier for the warm SSTA to reach the threshold for deep convections (Gadgil et al. 1984; Graham and Barnett 1987; Waliser and Graham 1993) and therefore more effectively to drive wind changes (Tanuma and Tozuka 2020). As a result, the large-scale cyclonic wind anomalies and the west-east SSTA dipole (Fig. 1) may tend to occur in the eastern Indian Ocean during the positive decadal WPD (warm southeast Indian Ocean and cold central-western tropical Pacific), leading to the eastward shift of the action center for the South Indian Ocean interannual climate variability. Once the interannual climate variability preferably occurs in the eastern part of the subtropical South Indian Ocean, the so-called coastal Bjerknes feedback may kick in (Tozuka et al. 2021), which primarily causes prominent SSTA in the coastal region through changes in the coastal upwelling and/or the Leeuwin current. Hence, although the decadal warm SSTA in the model are located west of the typical Ningaloo Niño region away from the coasts in the model (Fig. 7b), they may still favor development of Ningaloo Niño.

Changes in the remote influences from the Pacific forcing may also play a role. Indeed, we note significant increases in the SSTA SD in the central tropical Pacific Ocean in both observations and CESM1-LE, suggesting stronger ENSO variability (Figs. 4 and 7a). This may also contribute to the strengthening of Ningaloo Niño and Niña, since ENSO has strong influences on the southeast Indian Ocean through interbasin interactions via both the atmospheric and oceanic connections (Zhang and Han 2018). Previously, long-term alterations in ENSO variance have been attributed to the anthropogenic greenhouse gas forcing (Yeh et al. 2009) and the Atlantic Multidecadal Oscillation (AMO) (Yu et al. 2015). However, since the former effect has been excluded, and differences in the Atlantic SSTA in the CESM1-LE composites are weak (not shown), these two mechanisms cannot explain the enhanced ENSO variance that we found in CESM1-LE. Meanwhile, we also note that the tropical Indian Ocean SSTA SD has increased, which could be driven by the enhanced ENSO variance. However, since the tropical Indian and Pacific Oceans are intimately coupled together, causality of the changes in the two basins requires further investigation. On the other hand, the Pacific portion of the WPD resembles that of the Pacific Centennial Oscillation (Karnauskas et al. 2012; Samanta et al. 2018), which is associated with significant changes in ENSO amplitude with a weakened Pacific zonal SST gradient on centennial timescale corresponding to stronger ENSO variability. Hence, the decadal WPD may also modulate ENSO strength and subsequently affect the Ningaloo Niño variance.

4. Climate impacts of changes in SIOD and Ningaloo Niño

4.1 Rainfall changes

Climate modes are associated with distinct spatial patterns of precipitation in both local and remote regions (Figs. 9d-f). For instance, the positive SIOD is associated with dipole-like rainfall anomalies over the South Indian Ocean and above-average rainfall over southern Africa during austral summer. By contrast, the effect of Ningaloo Niño on rainfall is mainly confined to the central tropical

Indian Ocean and the eastern basin. In addition, ENSO as the dominant interannual climate mode on the planet (McPhaden et al. 2006) can also induce significant climate anomalies over the South Indian Ocean region (Xie et al. 2002), and it has been suggested to affect the southern African rainfall, with El Niño corresponding to drying conditions in the region (Cane et al. 1994). Furthermore, the three climate modes exhibit similar patterns of associated climate anomalies prior to and after 1985, except with different magnitudes (Fig. S8). While the SIOD and ENSO exhibit more prominent rainfall anomalies in recent decades, Ningaloo Niño is accompanied by more significant changes in rainfall over the eastern subtropical Indian Ocean and weaker rainfall anomalies over the central South Indian Ocean.

On interannual timescale, the strongest rainfall variability center is located at the south tropical Indian Ocean Intertropical convergence zone (ITCZ) and the North Indian Ocean monsoon region (Figs. 9a-b). In recent decades, the rainfall SD has strengthened over the central subtropical South Indian Ocean and southern Africa (Fig. 9c). This seems primarily related to stronger ENSO variability, which can induce significant rainfall anomalies in those regions (Fig. 9e). Although the rainfall anomalies associated with the SIOD become stronger since 1985, the SIOD itself has weakened and therefore may not contribute to the strengthened rainfall SD in the region. Similarly, although Ningaloo Niño has strengthened, its associated rainfall anomalies become weaker over the central South Indian Ocean.

This result indicates changes in the relative roles of the SIOD and ENSO in causing South Indian Ocean and southern African rainfall anomalies in recent decades, which may subsequently affect the source of predictability. Indeed, by calculating the regression of SSTA on a rainfall index defined as rainfall anomalies averaged over southern Africa, we find that the southern African rainfall variability is more affected by the SIOD prior to the 1980s (Fig. 10a), while the ENSO influence has become more dominant in recent decades (Fig. 10b). This is also consistent with a recent finding that the SIOD was a better predictor for the southern African rainfall for previous decades, while ENSO plays a more dominant role in recent decades (Harp et al. 2021). NCEP1 results agree with ERA-20C very well (Figs. S9-S11).

4.2 Sea level changes

Sea level variability and change affect millions of people living in the coastal and island regions (Han et al. 2019). Sea level is also a good proxy for the upper ocean heat content, and therefore can provide useful information for the ocean subsurface thermal variations. The strongest sea level variability in the Indian Ocean is generally found at the so-called Seychelles–Chagos thermocline ridge (SCTR) region where the mean thermocline depth is shallow (Hermes and Reason 2008; Yokoi et al. 2008) and the coastal upwelling region to the west of Sumatra and Java (Fig. 11a). In recent decades, the sea level variability has significantly strengthened at the SCTR and shifted eastward in the southern tropical Indian Ocean (Fig. 11b), and has become more prominent along the western Australian coast (Figs. 11b and 11c). The enhanced sea level SD at the SCTR region is likely associated with the eastward extension of the SCTR in recent decades, which has been attributed to changes in both local winds and remote Pacific forcing through oceanic waves (Rahul and Gnanaseelan 2016).

These changes in the sea level SD are also related to changes in the SIOD and Ningaloo Niño. Note that the SIOD is mainly associated with a north-south dipole-like sea level anomaly pattern at the SCTR and southeast of Madagascar (Fig. 11d) (Zhang et al. 2019b), while the sea level anomalies associated with Ningaloo Niño is confined to the eastern basin with negligible signals in the SCTR region (Fig. 11f). ENSO influences on the Indian Ocean sea level can be found at both the SCTR and the southeast Indian Ocean (Fig. 11e), and it has been suggested that the Pacific influences on Indian Ocean sea level variability are mainly through modulating Indian Ocean winds via the atmospheric bridge, while the oceanic pathway through the ITF primarily affects the South Indian Ocean sea level on decadal timescales (Deepa et al. 2018, 2019). Interestingly, sea level anomalies associated with all three climate modes have become stronger in recent decades (Fig. S12). Meanwhile, since Ningaloo Niño itself has been strengthening while the SIOD has been weakening, their associated sea level variabilities may change correspondingly. As a result, stronger sea level variations are found in the eastern basin coastal region while those in the western basin are weakened (Fig. 11c). Such a change in the pattern of the overall sea level variability may provide important information for disaster preparedness associated with extreme sea level rise. Overall, satellite-derived sea level product in recent decades agree with the ORAS4 data, but with weaker amplitude (Fig. S13).

5. Summary and discussion

The SIOD and Ningaloo Niño are the two dominant modes of interannual climate variability in the South Indian Ocean, both characterized by large-scale cyclonic wind anomalies on top of a dipole-like SSTA pattern (Fig. 1). Observations robustly show that the SIOD has been weakening while Ningaloo Niño has been strengthening in recent decades (Fig. 2). Correspondingly, the maximum SSTA SD center, defined as the action center, has been shifting from the western-central basin to the eastern basin coastal region in the subtropical South Indian Ocean (Fig. 3).

By analyzing CESM1 experiments, we investigate the cause for these recent opposite changes in the two climate modes. Ensemble-mean results from the CESM1 large-ensemble (CESM1-LE), which are solely due to the external forcing, show too weak changes in the SIOD and Ningaloo Niño compared to observations (Fig. 6). The spread across different CESM1-LE ensemble members is also large. These results suggest that the observed changes in the two climate modes are due to influences of internal climate variability.

On the other hand, the CESM1 POGA experiment that isolates the effect of the central-eastern Pacific SSTA forcing cannot reproduce the contrasting changes in the SIOD and Ningaloo Niño, suggesting that the tropical Pacific natural climate variability such as the IPO may not play a dominant role. Consistently, the IPO in observations transited from negative to positive phase in the late 1970s, and returned back to negative phase in the early 2000s (Zhang 2016; Zhang et al. 2018b; Han et al. 2014a), during which time the large SSTA SD center in the subtropical South Indian Ocean exhibits a persistent eastward shift (Fig. 3). In addition, it has been reported that while the IPO may affect the tropical Indian Ocean prior to the 1980s, this remote influence has become insignificant in recent decades (Zhang et al. 2018b; Mohapatra et al. 2020). Hence, it seems unlikely that the IPO contributes significantly to the recent changes in the amplitude of the SIOD and Ningaloo Niño. Similarly, the tropical Indian Ocean internal climate variability assessed by the ensemble mean of IOGA experiments cannot capture the observed changes in the South Indian Ocean interannual climate variability either.

By comparing the CESM1-LE members that do and do not simulate both the weakening of the SIOD and the strengthening of Ningaloo Niño, we find that such changes are associated with a decadal WPD SSTA pattern, with warm SSTA in the southeast Indian Ocean and cold SSTA in the western-central tropical Pacific (Fig. 7). The higher background SST in the southeast Indian Ocean associated with the positive decadal WPD prompts more active local air-sea interactions in the region, which favors the development of Ningaloo Niño and thus shifts the action center of the South Indian Ocean interannual climate variability toward the eastern basin. Stronger ENSO variance, which could also be linked to the decadal WPD (Karnauskas et al. 2012), may also contribute.

It is worth noting that current generation of climate models, including the CESM1, still has biases that may affect their ability of faithfully simulating climate variability and interbasin interactions. For instance, ENSO signals extend too further westward into the western Pacific warm pool in the model (e.g., Guilyardi et al. 2009), which may allow them to more effectively affect the tropical Indian Ocean. Indeed, it has been found that the CESM1 tends to simulate too a strong IOD response to ENSO

(Deser et al. 2012). This could be the reason why we find a prominent negative IOD pattern during Ningaloo Niño in the model (Fig. 5a), which is likely caused by the Pacific La Niña-like SSTA. On the other hand, since our conclusion on the role of the tropical Indian Ocean forcing in affecting the South Indian Ocean is based upon analysis of CESM1 pacemaker experiment in which the SSTA in the tropical Indian Ocean is restored to observed values, influence of such model biases is reduced to some extent.

Impacts of the recent changes in the SIOD and Ningaloo Niño on climate conditions in the South Indian Ocean and surrounding regions are further analyzed. For instance, previous studies have suggested that both the SIOD and ENSO can affect the southern African rainfall (Fig. 9). Due to the recent weakening of the SIOD, rainfall variability over southern Africa is less affected by the local Indian Ocean forcing associated with southern Indian Ocean SSTA. Instead, the remote ENSO forcing plays a more dominant role in causing southern African rainfall anomalies through the atmospheric teleconnection. Similarly, the contrasting changes in the amplitudes of the SIOD and Ningaloo Niño also alter the sea level SD pattern. While the strengthened Ningaloo Niño induces stronger sea level variability in the eastern basin, the weakened SIOD leads to weaker sea level variability in the western basin in recent decades (Fig. 11). Since rainfall anomalies over southern Africa can affect local agriculture (e.g., Cane et al. 1994) and public health (e.g., Harp et al. 2021), and coastal sea level anomalies may affect environmental conditions and flood risks, these findings may provide new guidance for disaster preparedness and thus benefit the society.

Results presented in this study suggest that the decadal WPD, a mode of internal climate variability, can affect the amplitudes of the Indo-Pacific interannual climate modes. As a result, when the decadal WPD transitions into negative phase (cold southeast Indian Ocean and warm western tropical Pacific), the action center for the South Indian Ocean climate variability may shift back to the basin interior, which can prominently affect climate conditions in the region as illustrated above. Hence, findings in this study provide a new source of decadal predictability, which may help improve the climate prediction for the South Indian Ocean and surrounding regions.

Finally, while the physical mechanisms for the formation of the WPD on the interannual timescale have been explored (Zhang and Han 2018), the causes for the decadal WPD require further investigation. In Zhang and Han (2018), it has been suggested that warm SSTA in the southeast Indian Ocean and the cold SSTA in the central-western tropical Pacific are connected and can amplify each other through both the atmospheric bridge and the oceanic connection. However, this interbasin coupled mechanism may primarily work on the interannual timescale, and whether it also operates in a similar way for the decadal WPD remains unclear. A future study that specifically focuses on analyzing the associated physical processes for the development of the decadal WPD is warranted.

Acknowledgement

We thank the three anonymous reviewers for their constructive comments. L. Zhang and W. Han are supported by NSF AGS 1935279, NSF OCE 1658132 and NASA Ocean Surface Topography Science Team xxx. Y. L. is supported by the National Key R&D Program of China (2019YFA0606702) and Shandong Provincial Natural Science Foundation (ZR2020JQ17). We would like to thank Dr. Nan Rosenbloom from NCAR for her help with the CESM pacemaker experiments. We also would like to acknowledge high-performance computing support from Cheyenne (doi:10.5065/D6RX99HX) provided by NCAR's Computational and Information Systems Laboratory, sponsored by the National Science Foundation. All observational data and CESM1-LE results used in this study are available online. CESM1 pacemaker experiment results are available from corresponding author upon request.

References

Balmaseda, M. A., K. Mogensen, and A. T. Weaver, 2013: Evaluation of the ECMWF ocean reanalysis system ORAS4. *Q. J. R. Meteorol. Soc.*, **139**, 1132–1161, https://doi.org/10.1002/qj.2063.

Behera, S. K., and T. Yamagata, 2001: Subtropical SST dipole events in the southern Indian Ocean. *Geophys. Res. Lett.*, **28**, 327–330.

Byrne, M., 2011: Impact of ocean warming and ocean acidification on marine invertebrate life history stages: vulnerabilities and potential for persistence in a changing ocean. *Oceanogr. Mar. Biol. An Annu. Rev.*, **49**, 1–42, https://doi.org/10.1201/b11009-2.

Cai, W., and Coauthors, 2019: Pantropical climate interactions. *Science (80-.).*, **363**, eaav4236, https://doi.org/10.1126/science.aav4236.

Cane, M. A., G. Eshel, and R. W. Buckland, 1994: Forecasting Zimbabwean maize yield using eastern equatorial Pacific sea surface temperature. *Nature*, **370**, 204–205, https://doi.org/10.1038/370204a0.

Caputi, N., G. Jackson, and A. Pearce, 2014: *The marine heat wave off Western Australia during the summer of 2010/11 – 2 years on Management implications of climate change effects on fisheries in WA: an example of an extreme event*. 40 pp.

Clarke, A. J., and X. Liu, 1994: Interannual Sea Level in the Northern and Eastern Indian Ocean. *J. Phys. Oceanogr.*, **24**, 1224–1235, https://doi.org/10.1175/1520-0485(1994)024<1224:ISLITN>2.0.CO;2.

Deepa, J. S., C. Gnanaseelan, R. Kakatkar, A. Parekh, and J. S. Chowdary, 2018: The interannual sea level variability in the Indian ocean as simulated by an ocean general circulation model. *Int. J. Climatol.*, **38**, 1132–1144, https://doi.org/10.1002/joc.5228.

——, ——, S. Mohapatra, J. S. Chowdary, A. Karmakar, R. Kakatkar, and A. Parekh, 2019: The Tropical Indian Ocean decadal sea level response to the Pacific Decadal Oscillation forcing. *Clim. Dyn.*, **52**, 5045–5058, https://doi.org/10.1007/s00382-018-4431-9.

Denniston, R. F., and Coauthors, 2015: Extreme rainfall activity in the Australian tropics reflects changes in the El Niño/Southern Oscillation over the last two millennia. *Proc. Natl. Acad. Sci.*, **112**, 4576–4581, https://doi.org/10.1073/pnas.1422270112.

Depczynski, M., and Coauthors, 2013: Bleaching, coral mortality and subsequent survivorship on a West Australian fringing reef. *Coral Reefs*, **32**, 233–238, https://doi.org/10.1007/s00338-012-0974-0.

Deser, C., and Coauthors, 2012: ENSO and pacific decadal variability in the community climate system model version 4. *J. Clim.*, **25**, 2622–2651, https://doi.org/10.1175/JCLI-D-11-00301.1.

Eyring, V., and Coauthors, 2013: Long-term ozone changes and associated climate impacts in CMIP5 simulations. *J. Geophys. Res. Atmos.*, **118**, 5029–5060, https://doi.org/10.1002/jgrd.50316.

Feng, J., T. Li, and W. Zhu, 2015a: Propagating and Nonpropagating MJO Events over Maritime Continent*. *J. Clim.*, **28**, 8430–8449, https://doi.org/10.1175/JCLI-D-15-0085.1.

Feng, M., M. J. McPhaden, S. P. Xie, and J. Hafner, 2013: La Niña forces unprecedented Leeuwin Current warming in 2011. *Sci. Rep.*, **3**, 1–9, https://doi.org/10.1038/srep01277.

——, H. H. Hendon, S. P. Xie, A. G. Marshall, A. Schiller, Y. Kosaka, N. Caputi, and A. Pearce, 2015b: Decadal increase in Ningaloo Niño since the late 1990s. *Geophys. Res. Lett.*, **42**, 104–112, https://doi.org/10.1002/2014GL062509.

——, N. Caputi, A. Chandrapavan, M. Chen, A. Hart, and M. Kangas, 2021: Multi-year marine cold-spells off the west coast of Australia and effects on fisheries. *J. Mar. Syst.*, **214**, 103473, https://doi.org/10.1016/j.jmarsys.2020.103473.

Gadgil, S., P. V. Joseph, and N. V. Joshi, 1984: Ocean–atmosphere coupling over monsoon regions. *Nature*, **312**, 141–143, https://doi.org/10.1038/312141a0.

Graham, N. E., and T. P. Barnett, 1987: Sea Surface Temperature, Surface Wind Divergence, and Convection over Tropical Oceans. *Science (80-.).*, **238**, 657–659, https://doi.org/10.1126/science.238.4827.657.

Guilyardi, E., A. Wittenberg, A. Fedorov, M. Collins, C. Wang, A. Capotondi, G. J. Van Oldenborgh, and T. Stockdale, 2009: Understanding El Nino in ocean–atmosphere general circulation models. *Bull. Amer. Meteor. Soc*, **90**, 325–340.

Guo, Y., Y. Li, F. Wang, Y. Wei, and Z. Rong, 2020: Processes Controlling Sea Surface Temperature Variability of Ningaloo Niño. *J. Clim.*, **33**, 4369–4389, https://doi.org/10.1175/JCLI-D-19-0698.1.

Han, W., and Coauthors, 2014a: Intensification of decadal and multi-decadal sea level variability in the western tropical Pacific during recent decades. *Clim. Dyn.*, **43**, 1357–1379, https://doi.org/10.1007/s00382-013-1951-1.

——, J. Vialard, M. J. McPhaden, T. Lee, Y. Masumoto, M. Feng, and W. P. M. de Ruijter, 2014b: Indian Ocean Decadal Variability: A Review. *Bull. Am. Meteorol. Soc.*, **95**, 1679–1703, https://doi.org/10.1175/bams-d-13-00028.1.

——, and Coauthors, 2019: Impacts of Basin-Scale Climate Modes on Coastal Sea Level: a Review. *Surv. Geophys.*, **40**, 1493–1541, https://doi.org/10.1007/s10712-019-09562-8.

Harp, R. D., J. M. Colborn, B. Candrinho, K. L. Colborn, L. Zhang, and K. B. Karnauskas, 2021: Interannual Climate Variability and Malaria in Mozambique. *GeoHealth*, **5**, 1–17, https://doi.org/10.1029/2020GH000322.

Hermes, J. C., and C. J. C. Reason, 2008: Annual cycle of the South Indian Ocean (Seychelles-Chagos) thermocline ridge in a regional ocean model. *J. Geophys. Res. Ocean.*, **113**, 1–10, https://doi.org/10.1029/2007JC004363.

Higgins, R. W., V. E. Kousky, and P. Xie, 2011: Extreme Precipitation Events in the South-Central United States during May and June 2010: Historical Perspective, Role of ENSO, and Trends. *J. Hydrometeorol.*, **12**, 1056–1070, https://doi.org/10.1175/jhm-d-10-05039.1.

Hoerling, M. P., and A. Kumar, 2002: Atmospheric Response Patterns Associated with Tropical Forcing. *J. Clim.*, **15**, 2184–2203, https://doi.org/10.1175/1520-0442(2002)015<2184:ARPAWT>2.0.CO;2.

Holbrook, N. J., A. Sen Gupta, E. C. J. Oliver, A. J. Hobday, J. A. Benthuysen, H. A. Scannell, D. A. Smale, and T. Wernberg, 2020: Keeping pace with marine heatwaves. *Nat. Rev. Earth Environ.*, **1**, 482–493, https://doi.org/10.1038/s43017-020-0068-4.

Hu, S., and A. V. Fedorov, 2019: Indian Ocean warming can strengthen the Atlantic meridional overturning circulation. *Nat. Clim. Chang.*, **9**, 747–751, https://doi.org/10.1038/s41558-019-0566-x.

Huang, B., and Coauthors, 2017: Extended reconstructed Sea surface temperature, Version 5 (ERSSTv5): Upgrades, validations, and intercomparisons. *J. Clim.*, **30**, 8179–8205, https://doi.org/10.1175/JCLI-D-16-0836.1.

Hurrell, J. W., and Coauthors, 2013: The Community Earth System Model: A Framework for Collaborative Research. *Bull. Am. Meteorol. Soc.*, 1339–1360, https://doi.org/10.1175/BAMS-D-12-00121.

Ishii, M., A. Shouji, S. Sugimoto, and T. Matsumoto, 2005: Objective analyses of sea-surface temperature and marine meteorological variables for the 20th century using ICOADS and the Kobe Collection. *Int. J. Climatol.*, **25**, 865–879, https://doi.org/10.1002/joc.1169.

Jin, F. F., J. Boucharel, and I. I. Lin, 2014: Eastern Pacific tropical cyclones intensified by El Ninõ delivery of subsurface ocean heat. *Nature*, **516**, 82–85, https://doi.org/10.1038/nature13958.

Kalnay, E., and Coauthors, 1996: The NCEP/NCAR 40-Year Reanalysis Project. *Bull. Am. Meteorol. Soc.*, **77**, 437–471, https://doi.org/10.1175/1520-0477(1996)077<0437:TNYRP>2.0.CO;2.

Karnauskas, K. B., J. E. Smerdon, R. Seager, and J. F. González-Rouco, 2012: A Pacific Centennial Oscillation Predicted by Coupled GCMs*. *J. Clim.*, **25**, 5943–5961, https://doi.org/10.1175/JCLI-D-11-00421.1.

Kataoka, T., T. Tozuka, S. Behera, and T. Yamagata, 2014: On the Ningaloo Niño/Niña. *Clim. Dyn.*, **43**, 1463–1482, https://doi.org/10.1007/s00382-013-1961-z.

Kay, J. E., and Coauthors, 2015: The community earth system model (CESM) large ensemble project : A community resource for studying climate change in the presence of internal climate variability. *Bull. Am. Meteorol. Soc.*, **96**, 1333–1349, https://doi.org/10.1175/BAMS-D-13-00255.1.

Lee, T., and M. J. McPhaden, 2010: Increasing intensity of El Niño in the central-equatorial Pacific. *Geophys. Res. Lett.*, **37**, https://doi.org/10.1029/2010GL044007.

Li, Y., W. Han, and L. Zhang, 2017: Enhanced Decadal Warming of the Southeast Indian Ocean During the Recent Global Surface Warming Slowdown. *Geophys. Res. Lett.*, **44**, 9876–9884, https://doi.org/10.1002/2017GL075050.

Lin, L., C. Chen, and M. Luo, 2018: Impacts of El Niño-Southern Oscillation on heat waves in the Indochina peninsula. *Atmos. Sci. Lett.*, **19**, e856, https://doi.org/10.1002/asl.856.

Luo, J.-J., W. Sasaki, and Y. Masumoto, 2012: Indian Ocean warming modulates Pacific climate change. *Proc. Natl. Acad. Sci.*, **109**, 18701–18706, https://doi.org/10.1073/pnas.1210239109.

Marsh, D. R., and Coauthors, 2013: Climate Change from 1850 to 2005 Simulated in CESM1(WACCM). *J. Clim.*, **26**, 7372–7391, https://doi.org/10.1175/JCLI-D-12-00558.1.

Marshall, A. G., H. H. Hendon, M. Feng, and A. Schiller, 2015: Initiation and amplification of the Ningaloo Niño. *Clim. Dyn.*, **45**, 2367–2385, https://doi.org/10.1007/s00382-015-2477-5.

McPhaden, M. J., S. E. Zebiak, and M. H. Glantz, 2006: ENSO as an integrating concept in earth science. *Science (80-.).*, **314**, 1740–1745, https://doi.org/10.1126/science.1132588.

Meyers, G., 1996: Variation of Indonesian throughflow and the El Niño-Southern Oscillation. *J. Geophys. Res. Ocean.*, **101**, 12255–12263, https://doi.org/10.1029/95JC03729.

Mohapatra, S., C. Gnanaseelan, and J. S. Deepa, 2020: Multidecadal to decadal variability in the equatorial Indian Ocean subsurface temperature and the forcing mechanisms. *Clim. Dyn.*, **54**, 3475–3487, https://doi.org/10.1007/s00382-020-05185-7.

Pearce, A. F., and M. Feng, 2013: The rise and fall of the "marine heat wave" off Western Australia during the summer of 2010/2011. *J. Mar. Syst.*, **111–112**, 139–156, https://doi.org/10.1016/j.jmarsys.2012.10.009.

Poli, P., and Coauthors, 2016: ERA-20C: An atmospheric reanalysis of the twentieth century. *J. Clim.*, **29**, 4083–4097, https://doi.org/10.1175/JCLI-D-15-0556.1.

Rahul, S., and C. Gnanaseelan, 2016: Can large scale surface circulation changes modulate the sea surface warming pattern in the Tropical Indian Ocean? *Clim. Dyn.*, **46**, 3617–3632, https://doi.org/10.1007/s00382-015-2790-z.

Ratnam, J. V., S. K. Behera, H. Annamalai, S. B. Ratna, M. Rajeevan, and T. Yamagata, 2016: ENSO's far reaching connection to Indian cold waves. *Sci. Rep.*, **6**, 37657, https://doi.org/10.1038/srep37657.

Rayner, N. A., D. E. Parker, E. B. Horton, C. K. Folland, L. V. Alexander, D. P. Rowell, E. C. Kent, and A. Kaplan, 2003: Global analyses of sea surface temperature, sea ice, and night marine air temperature since the late nineteenth century. *J. Geophys. Res.*, **108**, 4407, https://doi.org/10.1029/2002JD002670.

Reason, C. J. C., 2001: Subtropical Indian Ocean SST dipole events and southern African rainfall. *Geophys. Res. Lett.*, **28**, 2225–2227, https://doi.org/10.1029/2000GL012735.

Saji, N. H., and T. Yamagata, 2003: Possible impacts of Indian Ocean Dipole mode events on global climate. *Clim. Res.*, **25**, 151–169, https://doi.org/10.3354/cr025151.

Saji, N. H., B. N. Goswami, P. N. Vinayachandran, and T. Yamagata, 1999: A dipole mode in the tropical Indian Ocean. *Nature*, **401**, 360–363, https://doi.org/10.1038/43854.

Samanta, D., K. B. Karnauskas, N. F. Goodkin, S. Coats, J. E. Smerdon, and L. Zhang, 2018: Coupled Model Biases Breed Spurious Low-Frequency Variability in the Tropical Pacific Ocean. *Geophys. Res. Lett.*, **45**, 10,609-10,618, https://doi.org/10.1029/2018GL079455.

Schneider, D. P., and C. Deser, 2018: Tropically driven and externally forced patterns of Antarctic sea ice change: reconciling observed and modeled trends. *Clim. Dyn.*, **50**, 4599–4618, https://doi.org/10.1007/s00382-017-3893-5.

——, ——, and T. Fan, 2015: Comparing the Impacts of Tropical SST Variability and Polar Stratospheric Ozone Loss on the Southern Ocean Westerly Winds*. *J. Clim.*, **28**, 9350–9372, https://doi.org/10.1175/JCLI-D-15-0090.1.

Tanuma, N., and T. Tozuka, 2020: Influences of the Interdecadal Pacific Oscillation on the Locally Amplified Ningaloo Niño. *Geophys. Res. Lett.*, **47**, 1–8, https://doi.org/10.1029/2020GL088712.

Tozuka, T., and P. Oettli, 2018: Asymmetric Cloud-Shortwave Radiation-Sea Surface Temperature Feedback of Ningaloo Niño/Niña. *Geophys. Res. Lett.*, **45**, 9870–9879, https://doi.org/10.1029/2018GL079869.

——, T. Kataoka, and T. Yamagata, 2014: Locally and remotely forced atmospheric circulation anomalies of Ningaloo Niño/Niña. *Clim. Dyn.*, **43**, 2197–2205, https://doi.org/10.1007/s00382-013-2044-x.

——, M. Feng, W. Han, S. Kido, and L. Zhang, 2021: The Ningaloo Niño/Niña: Mechanisms, relation with other climate modes and impacts. *Tropical and Extratropical Air-Sea Interactions*, Elsevier, 207–219.

Waliser, D. E., and N. E. Graham, 1993: Convective cloud systems and warm-pool sea surface temperatures: Coupled interactions and self-regulation. *J. Geophys. Res.*, **98**, 12881, https://doi.org/10.1029/93JD00872.

Wang, B., and J. C. L. Chan, 2002: How Strong ENSO Events Affect Tropical Storm Activity over the Western North Pacific*. *J. Clim.*, **15**, 1643–1658, https://doi.org/10.1175/1520-0442(2002)015<1643:HSEEAT>2.0.CO;2.

Webster, P. J., A. M. Moore, J. P. Loschnigg, and R. R. Leben, 1999: Coupled ocean–atmosphere dynamics in the Indian Ocean during 1997–98. *Nature*, **401**, 356–360, https://doi.org/10.1038/43848.

Xie, S. P., H. Annamalai, F. A. Schott, and J. P. McCreary, 2002: Structure and mechanisms of South Indian Ocean climate variability. *J. Clim.*, **15**, 864–878, https://doi.org/10.1175/1520-0442(2002)015<0864:SAMOSI>2.0.CO;2.

——, K. Hu, J. Hafner, H. Tokinaga, Y. Du, G. Huang, and T. Sampe, 2009: Indian Ocean capacitor effect on Indo-Western pacific climate during the summer following El Niño. *J. Clim.*, **22**, 730–747, https://doi.org/10.1175/2008JCLI2544.1.

Yan, L., Y. Du, and L. Zhang, 2013: Southern ocean SST variability and its relationship with ENSO on inter-decadal time scales. *J. Ocean Univ. China*, **12**, 287–294, https://doi.org/10.1007/s11802-013-2262-1.

Yang, J., Q. Liu, S.-P. Xie, Z. Liu, and L. Wu, 2007: Impact of the Indian Ocean SST basin mode on the Asian summer monsoon. *Geophys. Res. Lett.*, **34**, L02708, https://doi.org/10.1029/2006GL028571.

Yeh, S. W., J. S. Kug, B. Dewitte, M. H. Kwon, B. P. Kirtman, and F. F. Jin, 2009: El Niño in a changing climate. *Nature*, **461**, 511–514, https://doi.org/10.1038/nature08316.

Yokoi, T., T. Tozuka, and T. Yamagata, 2008: Seasonal variation of the Seychelles Dome. *J. Clim.*, **21**, 3740–3754, https://doi.org/10.1175/2008JCLI1957.1.

Yu, J.-Y., P. Kao, H. Paek, H.-H. Hsu, C. Hung, M.-M. Lu, and S.-I. An, 2015: Linking Emergence of the Central Pacific El Niño to the Atlantic Multidecadal Oscillation. *J. Clim.*, **28**, 651–662, https://doi.org/10.1175/JCLI-D-14-00347.1.

Zhang, L., 2016: The roles of external forcing and natural variability in global warming hiatuses. *Clim. Dyn.*, **47**, 3157–3169, https://doi.org/10.1007/s00382-016-3018-6.

——, and W. Han, 2018: Impact of Ningaloo Niño on Tropical Pacific and an Interbasin Coupling Mechanism. *Geophys. Res. Lett.*, **45**, 11,300-11,309, https://doi.org/10.1029/2018GL078579.

——, and ——, 2020: Barrier for the Eastward Propagation of Madden-Julian Oscillation Over the Maritime Continent: A Possible New Mechanism. *Geophys. Res. Lett.*, **47**, https://doi.org/10.1029/2020GL090211.

——, ——, Y. Li, and T. Shinoda, 2018a: Mechanisms for Generation and Development of the

Ningaloo Niño. *J. Clim.*, **31**, 9239–9259, https://doi.org/10.1175/JCLI-D-18-0175.1.

——, ——, and F. Sienz, 2018b: Unraveling Causes for the Changing Behavior of the Tropical Indian Ocean in the Past Few Decades. *J. Clim.*, **31**, 2377–2388, https://doi.org/10.1175/JCLI-D-17-0445.1.

——, ——, K. B. Karnauskas, G. A. Meehl, A. Hu, N. Rosenbloom, and T. Shinoda, 2019a: Indian Ocean Warming Trend Reduces Pacific Warming Response to Anthropogenic Greenhouse Gases: An Interbasin Thermostat Mechanism. *Geophys. Res. Lett.*, **46**, 10882–10890, https://doi.org/10.1029/2019GL084088.

——, ——, Y. Li, and N. S. Lovenduski, 2019b: Variability of Sea Level and Upper-Ocean Heat Content in the Indian Ocean: Effects of Subtropical Indian Ocean Dipole and ENSO. *J. Clim.*, **32**, 7227–7245, https://doi.org/10.1175/JCLI-D-19-0167.1.

——, ——, ——, and ——, 2019c: Variability of sea level and upper-ocean heat content in the indian ocean: Effects of subtropical indian ocean dipole and enso. *J. Clim.*, **32**, 7227–7245, https://doi.org/10.1175/JCLI-D-19-0167.1.

——, G. Wang, M. Newman, and W. Han, 2021: Interannual to Decadal Variability of Tropical Indian Ocean Sea Surface Temperature: Pacific Influence versus Local Internal Variability. *J. Clim.*, **34**, 2669–2684, https://doi.org/10.1175/JCLI-D-20-0807.1.

Zinke, J., A. Rountrey, M. Feng, S. P. Xie, D. Dissard, K. Rankenburg, J. M. Lough, and M. T. McCulloch, 2014: Corals record long-term Leeuwin current variability including Ningaloo Niño/Niña since 1795. *Nat. Commun.*, **5**, 1–9, https://doi.org/10.1038/ncomms4607.

Figure captions

Figure 1 Regression of December-February (DJF) mean sea surface temperature anomalies (SSTA) (shading; ˚C) from HadISST for 1950-2018 and surface wind stress anomalies (vector; N m^{-2}) from ERA-20C for 1950-2010 on normalized DJF mean (a) Ningaloo Niño index (NNI) and (b) subtropical dipole mode index (SDMI). The signs in (b) are flipped. Shown are results that are statistically significant at the 90% confidence level. (c) Climatological mean of DJF SST and surface wind stress.

Figure 2 (a) Time evolution of DJF-mean normalized SDMI (blue) and NNI (red). The sign of SDMI is flipped. (b) Bars represent the 11-year running variance of DJF-mean normalized SDMI (blue) and NNI (red). Dashed line represents the 11-year running correlation between the SDMI and NNI. The sign of the correlation coefficient is flipped. (c) Differences of SSTA standard deviation during the two periods 1950-1985 and 1986-2018. Unit is ˚C. (a)-(c) are based on COBE1, and (d)-(f) and (g)-(i) are based on HadISST and ERSSTv5, respectively. Boxes in (c), (f), and (i) represent the regions for SDMI (purple) and NNI (blue) (see section 2).

Figure 3 Hovmöller diagram of 11-year running SSTA standard deviation averaged between 25˚S and 30˚S. Unit is ˚C. Shown are results using (a) COBE1, (b) HadISST, and (c) ERSSTv5. “X” marks the action center, which refers to the region where the SSTA SD is large.

Figure 4 (a)-(c) Differences of P2–P1 SSTA standard deviation (˚C) in three observational data. P1 and P2 represent the time periods1950-1985 and 1986-2018, respectively. (d)-(f) Same as (a)-(c) but for P2–P1 SSTA difference.

Figure 5 Same as Figures 1a, b, but for CESM1-LE results during 1950-2018 with ensemble mean signals removed prior to the regression analysis. Shown are the average of regression results from the forty ensemble members.

Figure 6 (a) Left panel shows differences of SSTA standard deviation (˚C) between the two periods 1950-1985 and 1986-2018 in CESM1-LE. Shown are ensemble mean differences of forty members. In the right panel, red symbols represent differences of SSTA standard deviation averaged in the Ningaloo Niño region (dashed box in the left panel), and blue symbols for the south Indian Ocean region (SIO; solid box in the left panel for the region in 55˚E-80˚E and 37˚S-27˚S). Boxplots represent the spread across CESM1-LE ensemble members for the two regions. The bar denotes the 75th, median, and the 25th percentile from top to bottom, and the line denotes the 90th and 10th percentile values. Circle and cross represent the median and mean values, respectively. Red and blue symbols represent observed changes in the NNI and SIOD from HadISST (triangle) ERSSTv5 (square) and COBE SST (circle), respectively. (b)(c) Left panel shows the differences of the standard deviation of the ensemble mean SSTAs in POGA and IOGA. Right panel is the same as (a) but for POGA and IOGA results, respectively. Ensemble mean SSTAs of CESM1-LE have been removed from each member of the two pacemaker experiments prior to calculation of SSTA SD. The SSTA nudging region in IOGA has been masked out in (c).

Figure 7 (a) Differences of P2–P1 SSTA standard deviation (˚C) in CESM1-LE. P1 and P2 represent the time periods1950-1985 and 1986-2018, respectively. The forty members are first ranked by the difference of standard deviation between the south Indian Ocean (solid box; 55˚E-80˚E and 37˚S-27˚S) and the Ningaloo Niño region (dashed box), and shown are the differences between the top 20% and bottom 20% members (8 members each). (b) Same as (a) but for P2–P1 SSTA difference between the two groups of CESM1-LE members. Stippling represents differences that are statistically significant at the 90% confidence level.

Figure 8 Hovmöller diagram of 11-year running SSTA standard deviation averaged between 27˚S and 37˚S. Shown are differences between the top 20% and bottom 20% members (8 members each) from CESM1-LE, the ensemble members of which are ranked by the difference of standard deviation between the south Indian Ocean and the Ningaloo Niño region (see Fig. 6). Unit is ˚C.

Figure 9 (a)(b) Standard deviation of precipitation anomalies (mm day^{-1}) during 1950-1985 and 1986-2010, respectively. Precipitation data is from ERA-20C. (c) Differences between (a) and (b). (d) Regression of DJF-mean precipitation anomalies on the normalized DJF SDMI from HadISST. (e)(f) Same as (d), but for regression on Niño-3 index and NNI, respectively. Stippling represents anomalies that are statistically significant at the 90% confidence level.

Figure 10 (a) Regression of DJF-mean SSTA (˚C) on normalized DJF precipitation anomalies averaged over southern Africa (blue box; 20˚E-40˚E, 30˚S-15˚S) for the period 1950-1985. SST data is from HadISST and precipitation data is from ERA-20C. (b) As in (a) but for 1986-2010. The Pacific box denotes the Niño-3 region (150˚W-90˚W; 5˚N-5˚S). Stippling represents anomalies that are statistically significant at the 90% confidence level.

Figure 11 Same as Figure 9, but for ORAS4 sea level anomalies during 1958-1985 and 1986-2017. Unit is cm. Stippling represents anomalies that are statistically significant at the 90% confidence level.

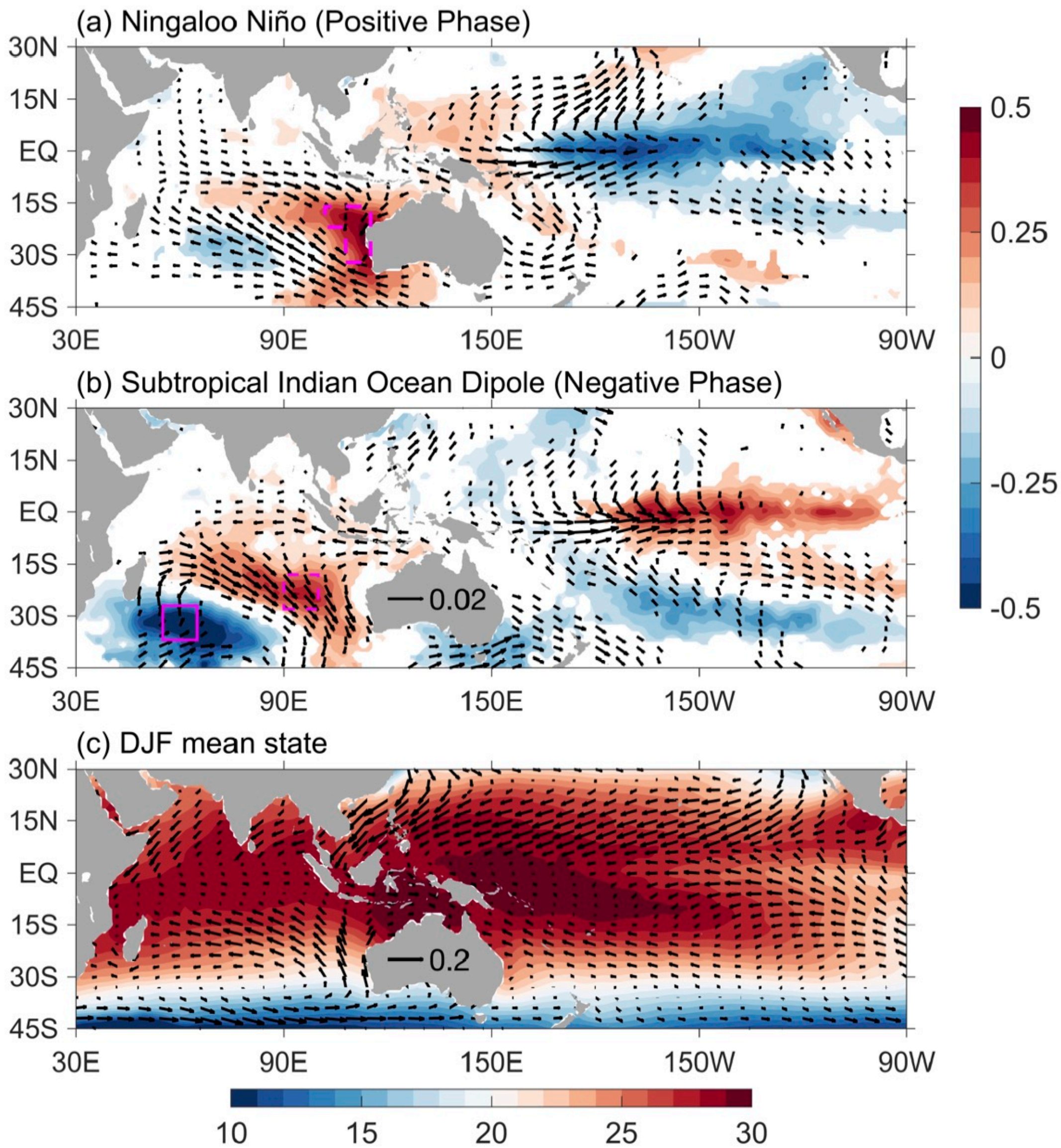

Figure 1 Regression of December-February (DJF) mean sea surface temperature anomalies (SSTA) (shading; ˚C) from HadISST for 1950-2018 and surface wind stress anomalies (vector; N m^{-2}) from ERA-20C for 1950-2010 on normalized DJF mean (a) Ningaloo Niño index (NNI) and (b) subtropical dipole mode index (SDMI). The signs in (b) are flipped. Shown are results that are statistically significant at the 90% confidence level. (c) Climatological mean of DJF SST and surface wind stress.

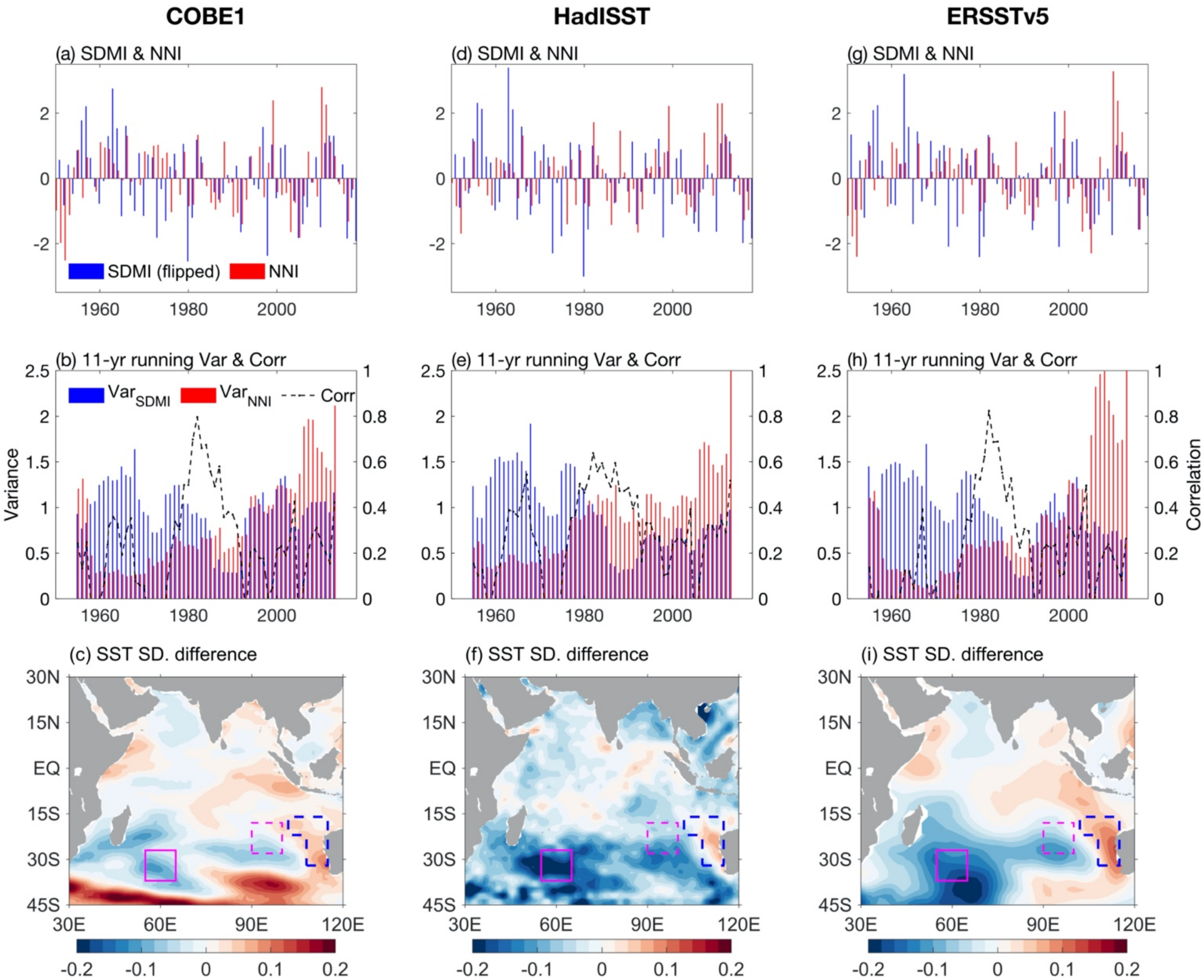

Figure 2 (a) Time evolution of DJF-mean normalized SDMI (blue) and NNI (red). The sign of SDMI is flipped. (b) Bars represent the 11-year running variance of DJF-mean normalized SDMI (blue) and NNI (red). Dashed line represents the 11-year running correlation between the SDMI and NNI. The sign of the correlation coefficient is flipped. (c) Differences of SSTA standard deviation during the two periods 1950-1985 and 1986-2018. Unit is ˚C. (a)-(c) are based on COBE1, and (d)-(f) and (g)-(i) are based on HadISST and ERSSTv5, respectively. Boxes in (c), (f), and (i) represent the regions for SDMI (purple) and NNI (blue) (see section 2).

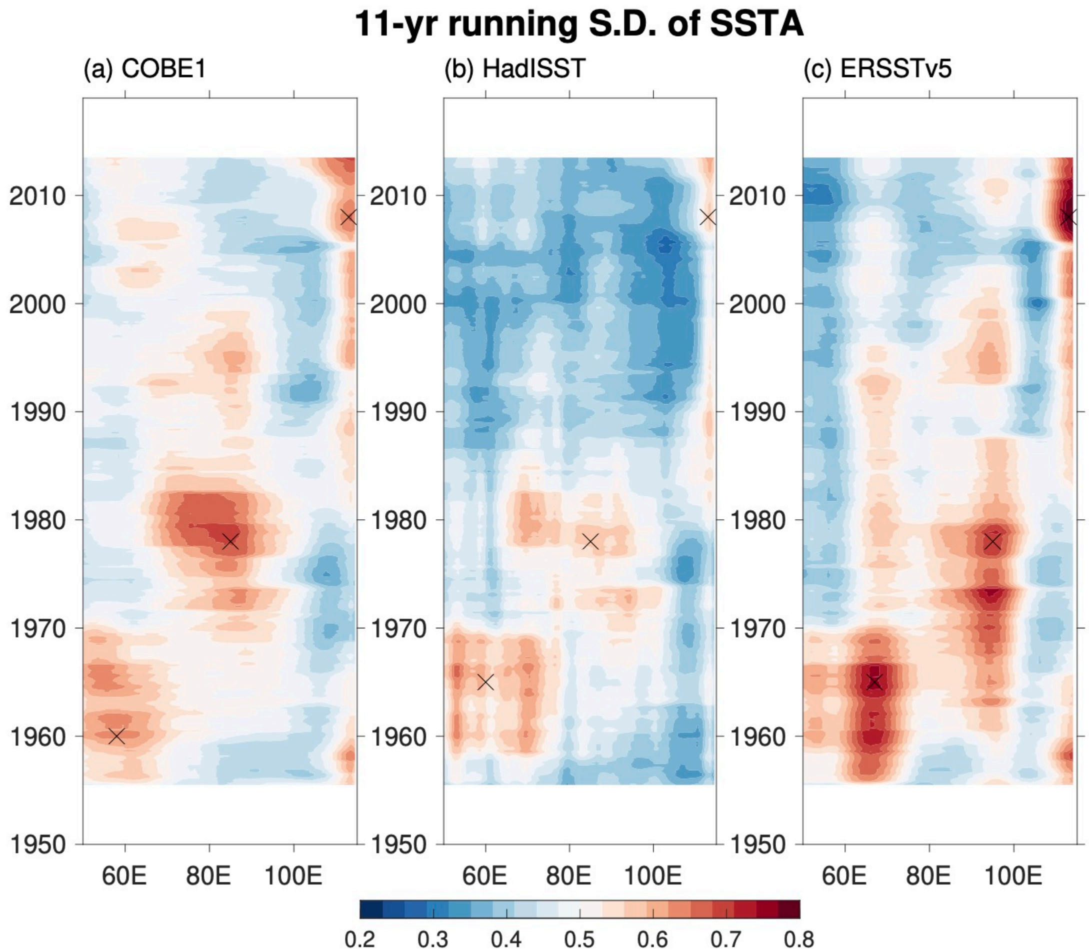

Figure 3 Hovmöller diagram of 11-year running SSTA standard deviation averaged between 25˚S and 30˚S. Unit is ˚C. Shown are results using (a) COBE1, (b) HadISST, and (c) ERSSTv5. "X" marks the action center, which refers to the region where the SSTA SD is large.

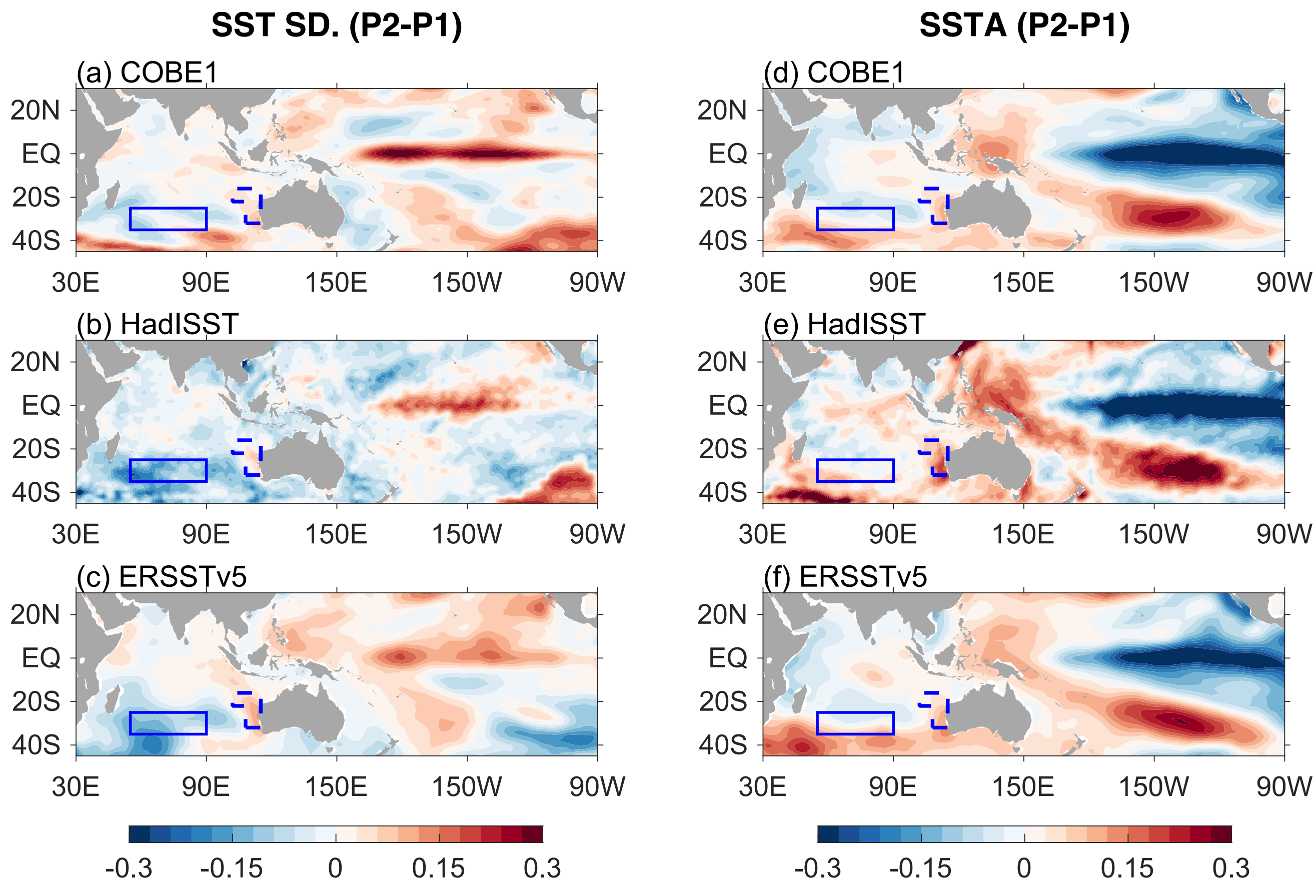

Figure 4 (a)-(c) Differences of P2–P1 SSTA standard deviation (˚C) in three observational data. P1 and P2 represent the time periods1950-1985 and 1986-2018, respectively. (d)-(f) Same as (a)-(c) but for P2–P1 SSTA difference.

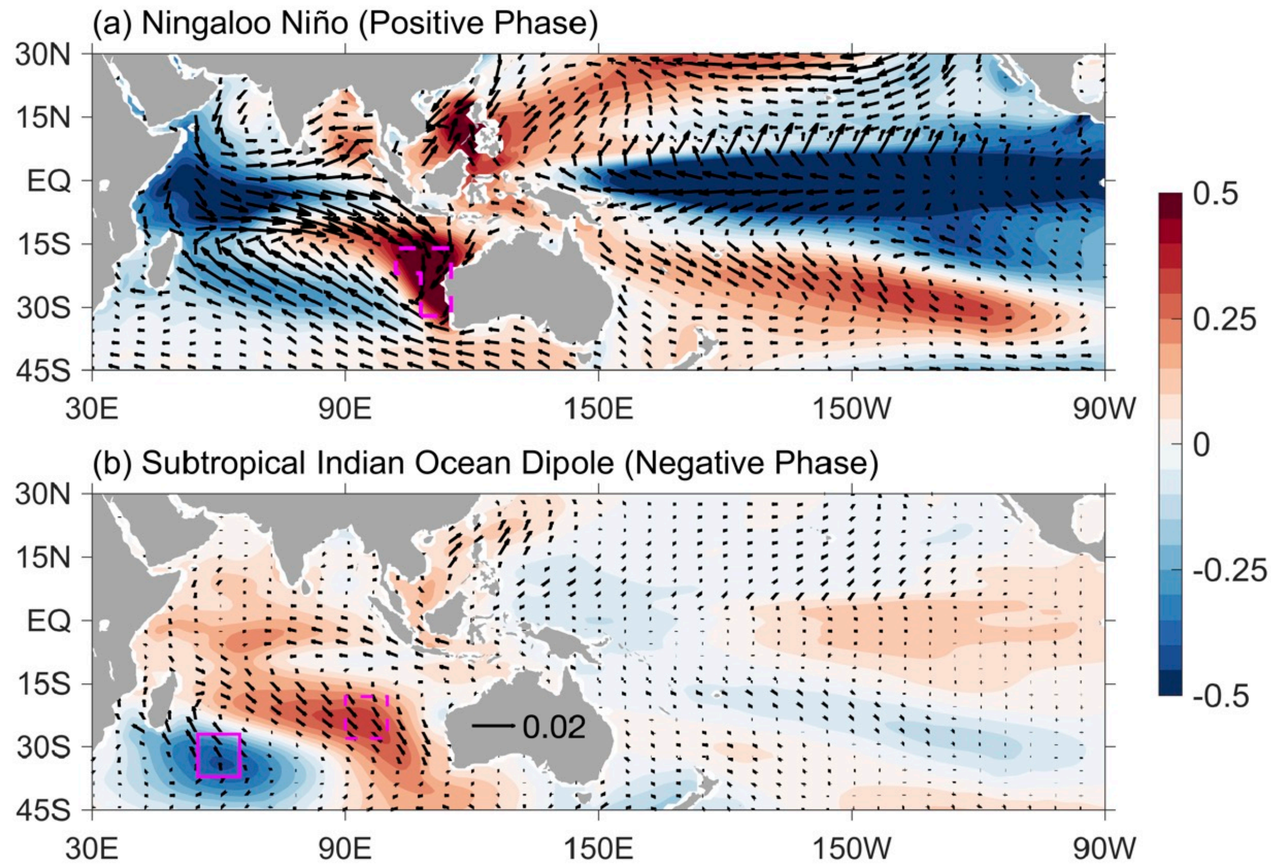

Figure 5 Same as Figures 1a, b, but for CESM1-LE results during 1950-2018 with ensemble mean signals removed prior to the regression analysis. Shown are the average of regression results from the forty ensemble members.

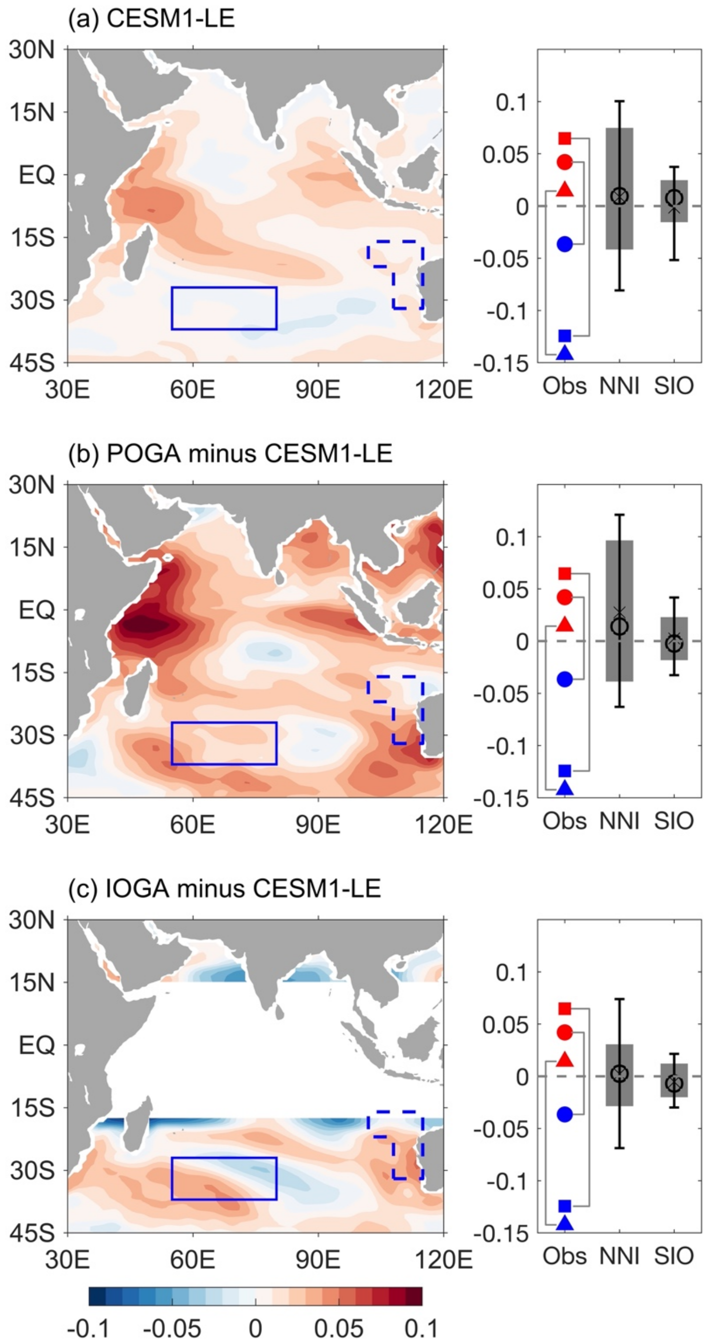

Figure 6 (a) Left panel shows differences of SSTA standard deviation (˚C) between the two periods 1950-1985 and 1986-2018 in CESM1-LE. Shown are ensemble mean differences of forty members. In the right panel, red symbols represent differences of SSTA standard deviation averaged in the Ningaloo Niño region (dashed box in the left panel), and blue symbols for the south Indian Ocean region (SIO; solid box in the left panel for the region in 55˚E-80˚E and 37˚S-27˚S). Boxplots represent the spread across CESM1-LE ensemble members for the two regions. The bar denotes the 75th, median, and the 25th percentile from top to bottom, and the line denotes the 90th and 10th percentile values. Circle and cross represent the median and mean values, respectively. Red and blue symbols represent observed changes in the NNI and SIOD from HadISST (triangle) ERSSTv5 (square) and COBE SST (circle),

respectively. (b)(c) Left panel shows the differences of the standard deviation of the ensemble mean SSTAs in POGA and IOGA. Right panel is the same as (a) but for POGA and IOGA results, respectively. Ensemble mean SSTAs of CESM1-LE have been removed from each member of the two pacemaker experiments prior to calculation of SSTA SD. The SSTA nudging region in IOGA has been masked out in (c).

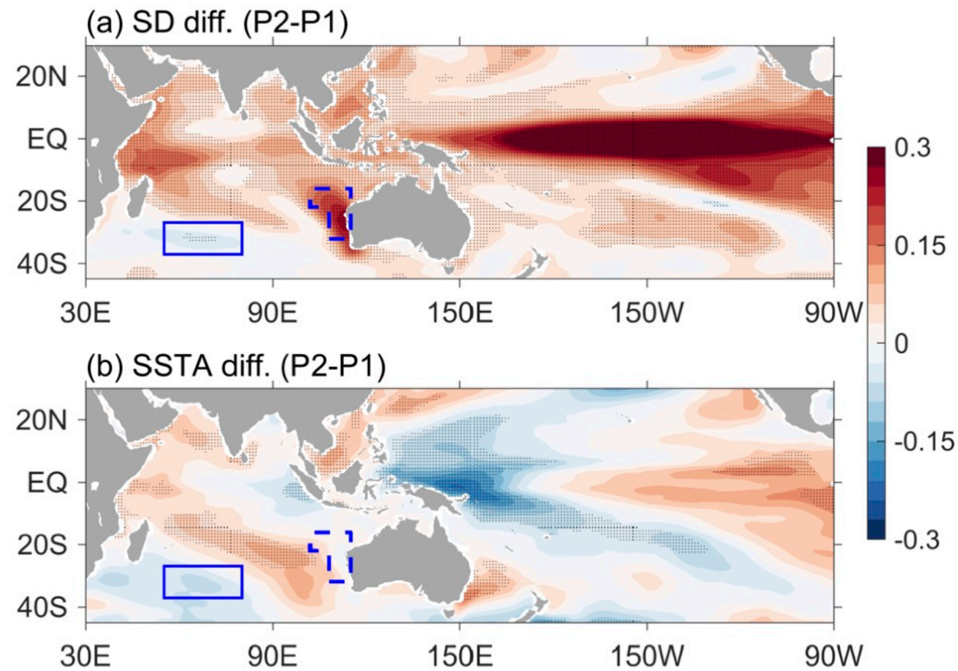

Figure 7 (a) Differences of P2–P1 SSTA standard deviation (˚C) in CESM1-LE. P1 and P2 represent the time periods1950-1985 and 1986-2018, respectively. The forty members are first ranked by the difference of standard deviation between the south Indian Ocean (solid box; 55˚E-80˚E and 37˚S-27˚S) and the Ningaloo Niño region (dashed box), and shown are the differences between the top 20% and bottom 20% members (8 members each). (b) Same as (a) but for P2–P1 SSTA difference between the two groups of CESM1-LE members. Stippling represents differences that are statistically significant at the 90% confidence level.

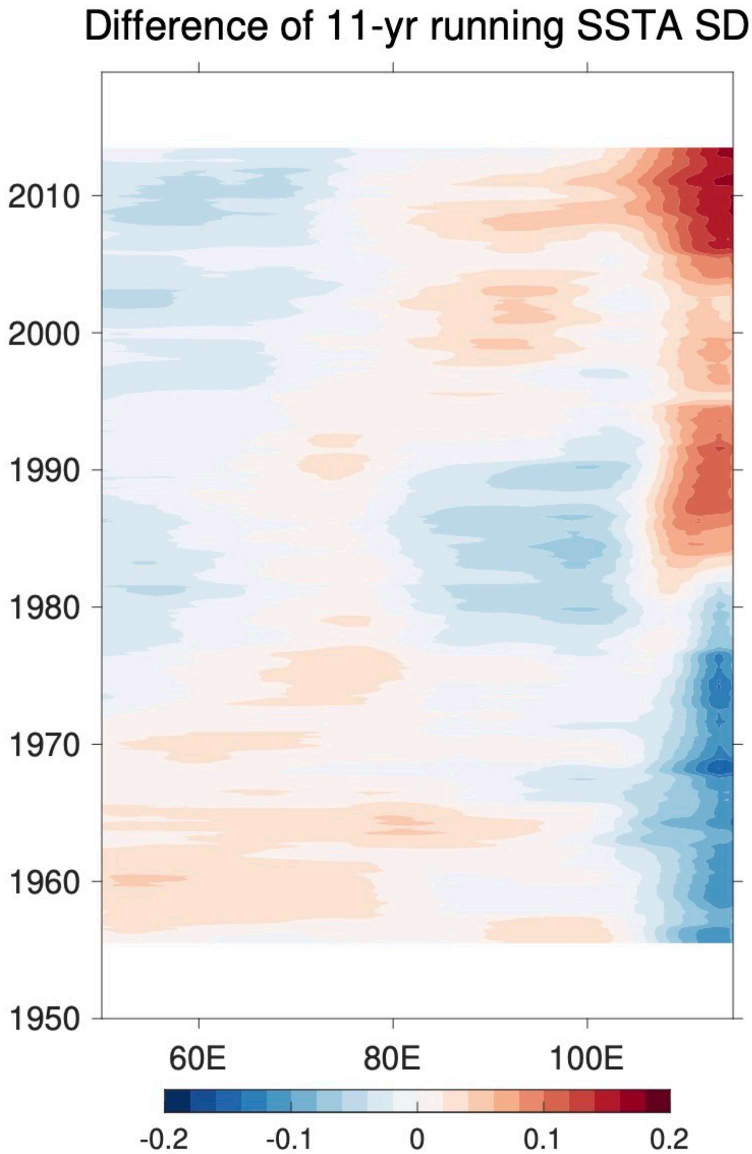

Figure 8 Hovmöller diagram of 11-year running SSTA standard deviation averaged between 27˚S and 37˚S. Shown are differences between the top 20% and bottom 20% members (8 members each) from CESM1-LE, the ensemble members of which are ranked by the difference of standard deviation between the south Indian Ocean and the Ningaloo Niño region (see Fig. 6). Unit is ˚C.

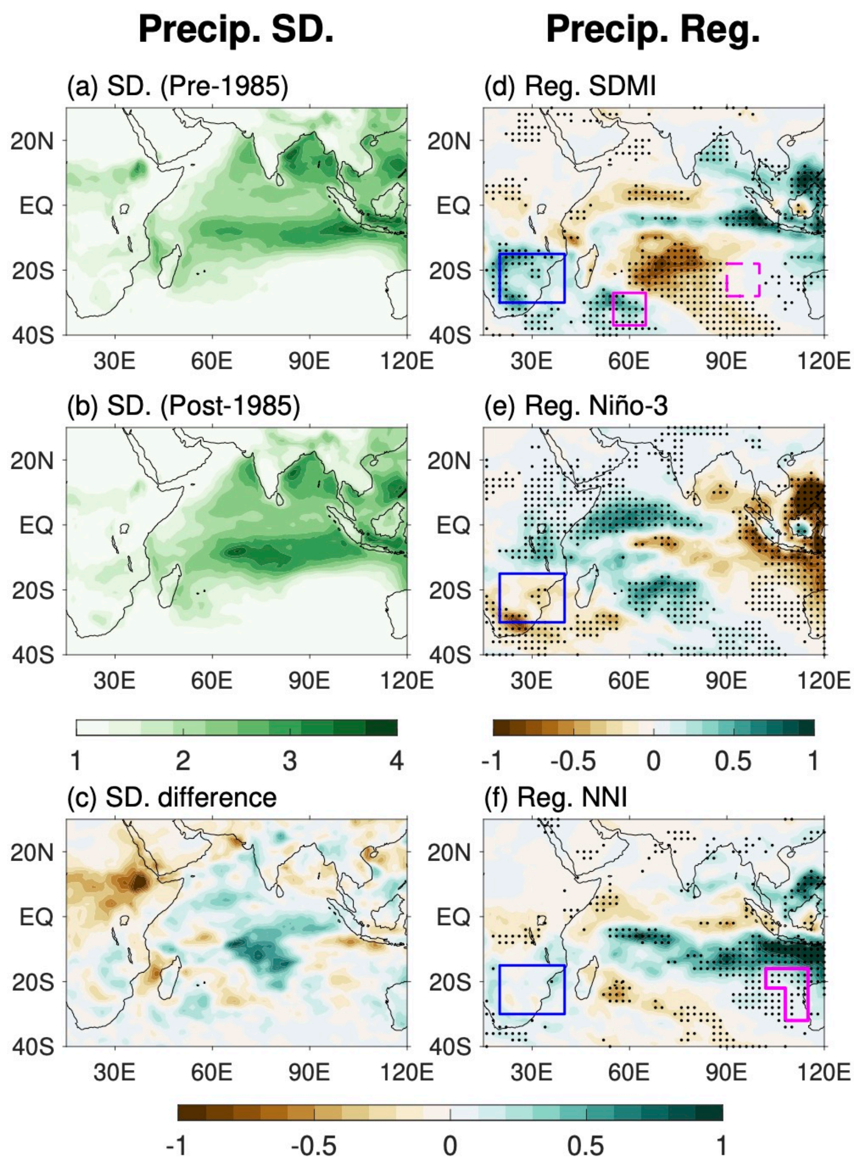

Figure 9 (a)(b) Standard deviation of precipitation anomalies (mm day^{-1}) during 1950-1985 and 1986-2010, respectively. Precipitation data is from ERA-20C. (c) Differences between (a) and (b). (d) Regression of DJF-mean precipitation anomalies on the normalized DJF SDMI from HadISST. (e)(f) Same as (d), but for regression on Niño-3 index and NNI, respectively. Stippling represents anomalies that are statistically significant at the 90% confidence level.

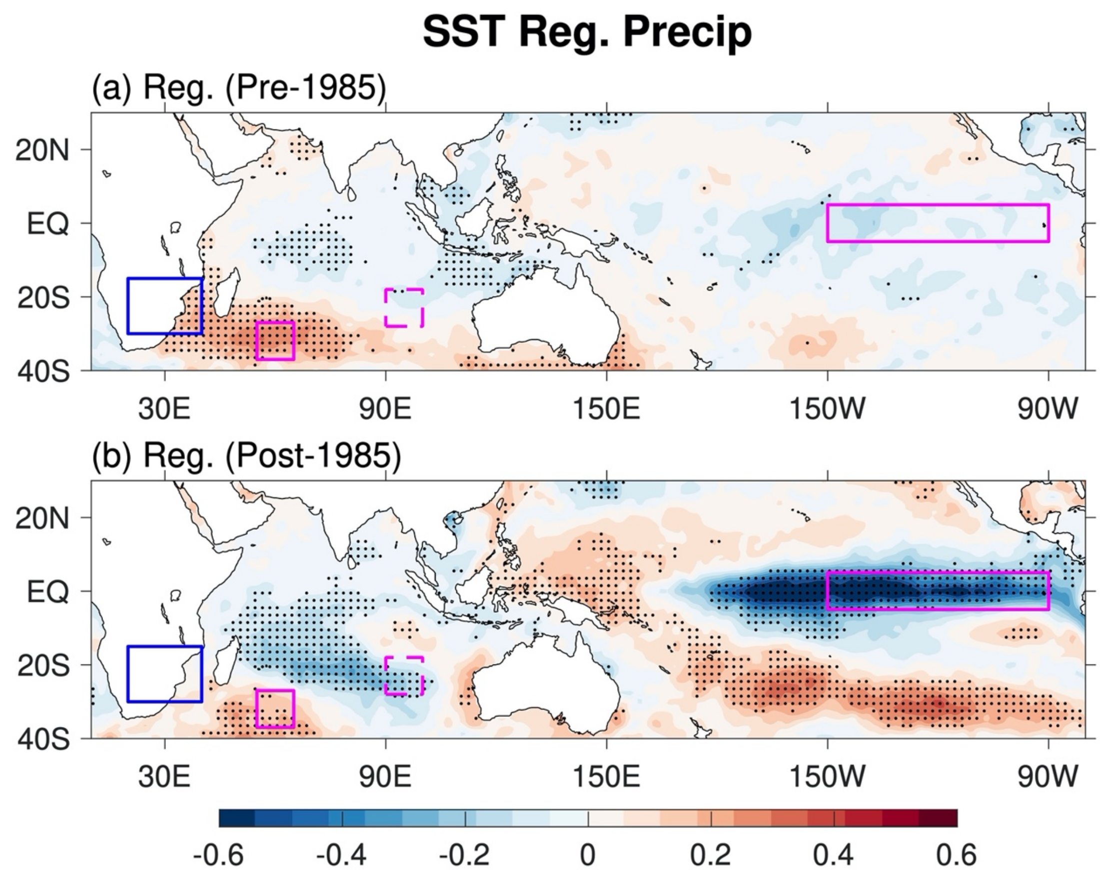

Figure 10 (a) Regression of DJF-mean SSTA (˚C) on normalized DJF precipitation anomalies averaged over southern Africa (blue box; 20˚E-40˚E, 30˚S-15˚S) for the period 1950-1985. SST data is from HadISST and precipitation data is from ERA-20C. (b) As in (a) but for 1986-2010. The Pacific box denotes the Niño-3 region (150˚W-90˚W; 5˚N-5˚S). Stippling represents anomalies that are statistically significant at the 90% confidence level.

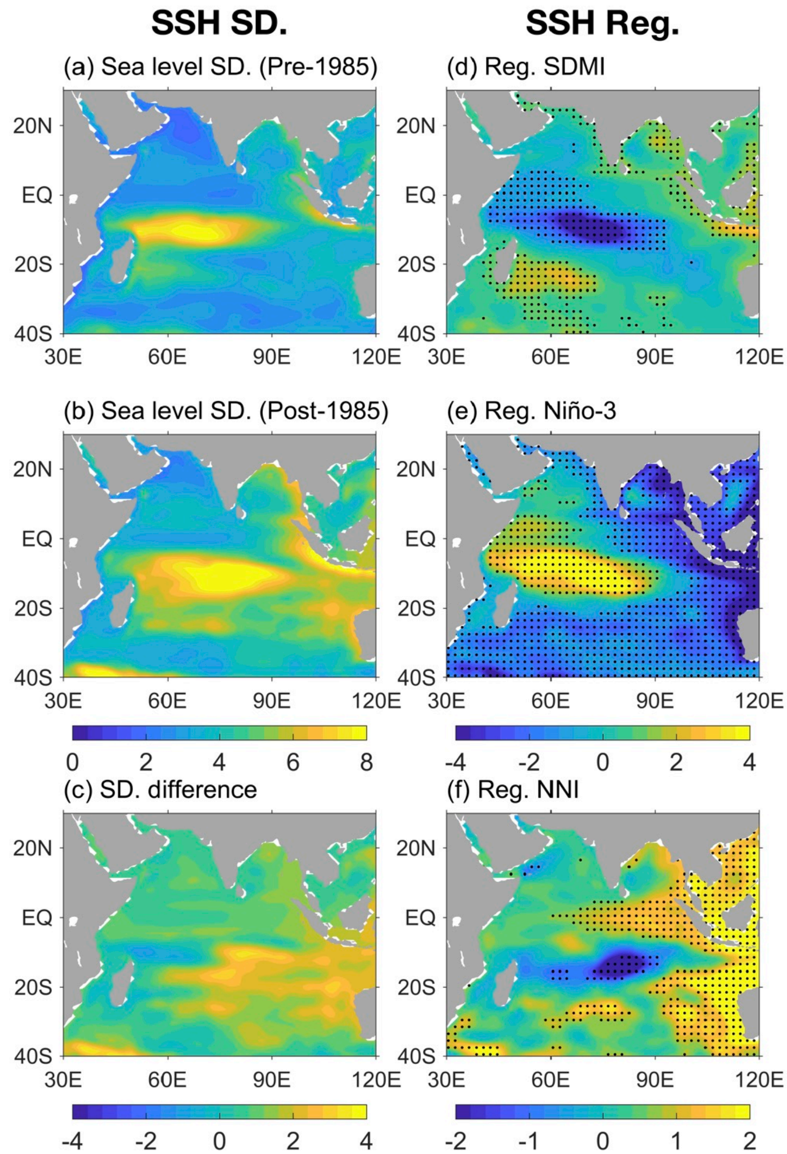

Figure 11 Same as Figure 9, but for ORAS4 sea level anomalies during 1958-1985 and 1986-2017. Unit is cm. Stippling represents anomalies that are statistically significant at the 90% confidence level.